Subliming GaN into Ordered Nanowire Arrays for Ultraviolet and Visible Nanophotonics

Sylvain Sergent, Benjamin Damilano, Stephane Vezian, Sébastien Chenot, Masato Takiguchi, Tai Tsuchizawa, Hideaki Taniyama, Masaya Notomi

Subliming GaN into ordered nanowire arrays for ultraviolet and visible nanophotonics

Sylvain Sergent,[1,2] Benjamin Damilano,[3,] Stéphane Vézian,[3] Sébastien Chenot,[3] Masato Takiguchi,[1,2] Tai Tsuchizawa, [1,4] Hideaki Taniyama,[1,2] and Masaya Notomi[1,2,**]*

[1]Nanophotonics Center, NTT Corp., 3-1, Morinosato Wakamiya, Atsugi, Kanagawa 243-0198, Japan

[2]NTT Basic Research Laboratories, NTT Corp., 3-1, Morinosato Wakamiya, Atsugi, Kanagawa 243-0198, Japan

[3]Université Côte d'Azur, CNRS, CRHEA, Rue B. Grégory, 06560 Valbonne, France

[4]NTT Device Technology Laboratory, NTT Corp., 3-1, Morinosato Wakamiya, Atsugi, Kanagawa 243-0198, Japan

ABSTRACT. We report on the fabrication of ordered arrays of InGaN/GaN nanowire quantum disks by a top-down selective-area sublimation method. Using a combination of two-dimensional molecular beam epitaxy of InGaN/GaN quantum wells, electron-beam lithography and ultra-high-vacuum sublimation techniques, we demonstrate that the position, geometry and dimensions of nanowires can be finely controlled at nano-, micro- and macro-scales. Relying on structural data, we evaluate in particular the relative sublimation rates of GaN crystal planes that

drive the nanowire formation, we assess the intrinsic limits of selective area sublimation for the fabrication of NW arrays and we evaluate the homogeneity of the process across the wafer. Because the sublimation method preserves the crystal quality of the NW material, we show that InGaN/GaN NWs present good optical properties, which can be leveraged for photonic applications in the ultraviolet and the visible range. In particular, we demonstrate that it is possible to realize on the same wafer not only arrays of nanowires that individually support room-temperature lasing based on Fabry-Pérot resonances, but also subwavelength nanowires that we integrate in photonic crystals for the realization of nanowire-induced nanocavities.

KEYWORDS. Nanowire, GaN, InGaN, quantum disk, quantum dot, selective-area sublimation, nanolaser, nanophotonics.

Group-III nitride nanowires (NWs) have recently emerged as candidates of choice for a large range of optoelectronics and photonics applications such as visible light-emitting diodes,[1-5] photodiodes,[6] photonic[7-9] and plasmonic[10-12] nanolasers, polariton lasers,[13] or even efficient single photon sources operating at high temperatures.[14,15] Despite such remarkable achievements, the fabrication of high-quality group-III nitride NWs with a fine control of their position, geometry and structural properties remains a challenge. Most of the literature on the topic has focused on bottom-up techniques based on molecular beam epitaxy (MBE)[16-19] or metal-organic chemical vapor deposition.[19-23] In order to maximize the structural quality of NWs, catalyst-free self-assembly growth processes have been widely used but such processes are intrinsically stochastic and make it difficult to control the position and geometry of NWs.[16-19] Using instead selective area growth on a patterned substrate allows to accurately position NWs.[20-23] It also gives more control over the NW diameter but because the overall geometry of NWs depends

directly on the kinetics of atoms adsorption and diffusion on existing surfaces, there remain significant constrains in controlling the diameter, aspect ratio and density of NWs all at once. Moreover, selective area growth is employed at the expense of the structural quality of NWs since the patterning process and exposure to air leads to unavoidable surface contaminations that are detrimental to the NW growth.

Instead of bottom-up growth processes, one can consider top-down fabrication techniques: there exists a number of attempts to realize arrays of NWs by a combination of patterning and etching processes on an epitaxially-grown stack[8,24,25] which allows the same kind of positioning control as the selective area growth approach. Wet etching is however poorly adapted for a fine control of the NW geometry because (i) aspect ratios are limited by the vertical to horizontal etching selectivity and (ii) local etching kinetics will strongly depend on the stack morphology and structural quality.[24] Dry etching approaches based on ion plasmas are much more reliable because they are less driven by chemical reactions and can be highly directional, allowing for a good diameter control and large aspect ratios. The main issue with the dry etching approach is that the ion plasma tends to damage the structural quality of the NW at etched surfaces, creating centers of non-radiative recombinations that are detrimental to optoelectronic and photonic applications. This drawback can be circumvented by wet etching of the damaged sidewalls in a potassium-based solution. In a significant technological development, Behzadirad *et al.* have recently shown that such a technique allows the realization of arrays of optically-pumped photon nanolasers.[8] The downsides of this fabrication method are however twofold: (i) the surface contamination and air exposure that occur during the NW processing limit the quality of any subsequent epitaxial growth and thus prevent the realization of core-shell structures or radial heterostructures with clean interfaces; (ii) the potassium-based wet etching rate depends on the

doping level, which inhibits the possibility to make NW p-n junctions with homogeneous diameters.

Alternatively, Damilano *et al.*[26,27] proposed a top-down technique based on the selective area sublimation of GaN in an ultra-high-vacuum environment. The technique has multiple advantages for the realization of group-III nitride NWs: (i) the sublimation of GaN is highly anisotropic, (ii) as opposed to dry etching processes it does not damage the NW sidewalls and do not require subsequent wet-etching cleaning, (iii) because the sublimation process is carried out in an ultra-high vacuum environment, epitaxial regrowth can be readily performed without exposure to air, enabling clean interfaces and high material quality. In their original paper, Damilano *et al.* realized randomly positioned NWs and demonstrated a limited control over the NW geometry and diameter. The technique was subsequently adapted to allow for NW positioning using either displacement Talbot lithography[28] or nanoimprint,[29] which respectively led to the demonstration of room-temperature Fabry-Pérot nanolasers and metalenses operating in the ultraviolet range. However there are significant limitations to the geometries, patterns and resolution that can be achieved by both Talbot lithography and nanoimprint. In this Article, we reveal that the sublimation technique can be significantly improved by using electron beam lithography in order to realize ordered arrays of GaN NWs embedding InGaN quantum disks. We first show that the technique leads to a high structural quality at a nano-scale, a good homogeneity at a micro-scale and a high yield at a macro-scale. We also show that it is possible to achieve a fine control of the position, geometry and diameter of NWs. This fine control allows us to evaluate the relative sublimation rates of GaN crystal planes that drive the nanowire formation and to assess the intrinsic limits of the selective-area sublimation process. We finally show that the good optical properties of NWs can be leveraged for nanophotonic applications in

the ultraviolet and visible range. In particular, we demonstrate that it is possible to realize on the same wafer not only arrays of NWs that can individually support room-temperature lasing based on Fabry-Pérot resonances, but also subwavelength NWs that we integrate in photonic crystals for the realization of nanowire-induced nanocavities.

RESULTS AND DISCUSSION

Fabrication Process. The NW fabrication process is schematically represented in Fig. 1a. GaN/AlGaN/GaN epilayer stacks are first grown on a (0001) sapphire substrate by molecular beam epitaxy. The lower GaN layer is 500 nm thick and constitutes the buffer layer. The 20 nm thick AlGaN layer is used both as an "etch stop" layer during the sublimation process. The upper GaN layer constitutes the material base for the NWs and includes a single InGaN quantum well at its center with a 12% nominal indium content and a 1.5 nm nominal thickness. The upper GaN thickness defines the final NW length and is set at L_{NW} = 4 μm. A 65-nm SiN hard mask layer is then deposited on top of the stack before spin-coating of a negative-tone resist. Arrays of triangular and hexagonal mesas are then defined by electron beam lithography in the resist (Fig. 1b). The mesa diameter, defined hereon as the diameter of the inscribed circle, is varied between 200 nm and 340 nm and the mesa sides are aligned with the $\{1\bar{1}00\}$ facets of GaN. The pitch of the NW arrays is 10 μm. The resist patterns are then transferred to the SiN hard mask by reactive ion etching and the sample is moved back into the molecular beam epitaxy reactor for NW formation by the selective-area sublimation of GaN. The sublimation process is carried out at 925°C in the ultrahigh vacuum environment of the reactor and the sample surface is monitored *in situ* and in real-time with a reflection high-energy electron diffraction (RHEED) apparatus, similarly to Reference 20. Because the sublimation rate of GaN depends on the crystallographic axis and is faster by orders of magnitude along the [0001] axis, the SiN mesas are expected to

efficiently protect the decomposition of the underlying GaN and allows for the formation of NWs with finely defined sections. During sublimation, the RHEED pattern shifts from streaky to spotty lines indicating a rapid change of the GaN surface from a two-dimensional to a rough three-dimensional surface. However, due to the low density of SiN mesas, vertical $\{1\bar{1}00\}$ facets evidencing the formation of NWs cannot be observed. The GaN is sublimated until the RHEED pattern retrieves a well-defined streaky line pattern evidencing the smooth two-dimensional surface of the "etch-stop" layer. Scanning electron microscope images (SEM) of the sample confirms the formation of arrays of 4-μm-long NWs (Fig. 1c) with well-defined triangular and hexagonal sections (Fig. 1d). Such fine features could not be achieved with previous masking techniques[26-29] and highlight one of the advantages of using electron beam lithography for this sublimation process. The SiN mask can be subsequently removed by hydrofluoric acid at room temperature with no damage to the NWs, as indicated by the well-preserved triangular and hexagonal sections shown in Fig. 1e.

Structural Properties. We first observe the effect of the sublimation process on the GaN crystal quality by transmission electron microscopy (TEM). TEM images of a NW cross-section show that the quality of the GaN single crystal is well preserved, even at the facets directly exposed to the sublimation process where no amorphous material can be observed (Figure 1f), as opposed to what is seen in plasma etching approaches[8,26]. Far from the sublimated facets we also observe the GaN/InGaN/GaN heterostructure by annular bright field scanning TEM along the $[1\bar{1}00]$ direction (Figure 1g). The TEM image confirms the single crystal nature of the InGaN quantum well and shows a fluctuating thickness with a 1.6 nm mean and a 0.2 nm standard deviation, *i.e.* close to the nominal thickness.

Hereafter, we draw from SEM images further insight into the sublimation process at nano-, micro- and macro-scales. We investigate 10×10 arrays of NWs and from the analysis of individual NW images (see Figure S1 in Supporting Information) we extract various geometric features: the SiN mesa diameter δ_{mesa}, the mean of the NW diameter δ along the NW axis, as well as the diameter fluctuation along the NW axis ν (Figure 2a). Owing to the reliability of the electron beam lithography and SiN dry etching processes, the array of triangular NWs of Fig. 1e stems from a very homogeneous set of mesas with a mean diameter value $\overline{\delta_{mesa}} = 203\ nm$ and a standard deviation $\sigma(\delta_{mesa}) = 7\ nm$. The NWs however present a larger inhomogeneity with a mean diameter $\bar{\delta} = 122\ nm$ and a standard deviation $\sigma(\delta) = 29\ nm$. This shows that the sublimation process induces some disorder most likely due to local disparities in the material quality, *i.e.* the presence of impurities and threading dislocations. The impact of dislocations on the geometric disorder of NWs may actually be limited considering the 5×10^9 cm^{-2} dislocation density estimated by TEM (Figure S2): depending on the NW diameter, this translates into only 1 to 3 dislocations per sublimated NW. Such disparities also induce fluctuations ν in the diameter of individual NWs along their axis: for the 100 NWs, we estimate the mean fluctuation to be limited to $\bar{\nu} = 13 \pm 6\ nm$ over their 4-µm length. Finally, we note that the NW diameter is consistently smaller than the mesa diameter, which shows that the lateral facet sublimation is not totally negligible. We thus infer the vertical to lateral sublimation ratio ρ for each NW and estimate its mean $\bar{\rho} = 1 \pm 0.4\%$. We perform the same structural study for arrays presenting mesa diameters ranging from 200 nm to 340 nm (See Figure S3 and S4 in Supporting Information) and show that we can finely control the NW diameter through the initial mesa diameter (Fig. 2b): the final mean NW diameter varies between 112nm and 260nm and individual NWs between 50nm and 300 nm, a diameter range that could not be achieved with

other masking techniques[26-29], showing the benefits of using electron beam lithography prior to the sublimation process. The NW and mesa diameters have a linear relationship of the form $\bar{\delta} = \overline{\delta_{mesa}} - 2\rho.L_{NW}$ with $2\rho.L_{NW} = 80 \pm 12nm$ according to a linear fitting to the data. For a NW length $L_{NW} = 4\mu m$, this confirms the value of the lateral to vertical sublimation ratio $\rho = 1 \pm 0.15\%$. Such a small value is the reason why NWs with such high aspect ratios can be formed, but it may still pose some constraint regarding NW array designs: in some extreme cases it may necessitate a tradeoff between the filling factor of the array, the NW diameter and the NW length. We finally estimate the macro-scale homogeneity of the sublimation process by measuring the fabrication yield of 170 arrays of 30×30 NWs obtained from the smallest mesa diameter $\overline{\delta_{mesa}}$~200nm. They are arguably the most fragile NWs and the most sensitive to material inhomogeneities and temperature variations. As can be seen in Fig. 2c, the fabrication yield is very high on most of the samples with a 98% average yield. Let us note that the fabrication yield tends to improve as the NW diameter increases. This high fabrication yield is a proof of the high reliability of the selective-area sublimation method, which is made possible by the homogeneous structural quality of the initial two-dimensional stack as well as the temperature uniformity on the wafer scale.

Optical Properties. The optical properties of NW arrays are investigated at room and cryogenic temperatures by microphotoluminescence (μPL). Room-temperature μPL measurements of individual NWs show intense emission in both the ultraviolet and the blue-violet ranges where GaN and InGaN are expected to emit (upper panel of Figure 3a). This intense room-temperature emission confirms that the sublimation process, as opposed to plasma etching techniques[8,26], does not significantly degrade the material quality and does not require an additional etching process to clean the NW sidewalls and recover optoelectronic activity. The room-temperature

μPL mapping of a 3×3 NW array (Figure 3b) unambiguously shows that the localized blue-violet emission emerges from the NWs embedding an InGaN quantum disk, whereas the ultraviolet GaN emission arises from both NWs and the underlying bulk GaN on the whole sample area. At room temperature, arrays of NWs are very homogeneous in terms of emission wavelength λ (see lower panel of Figure 3a, upper panel of Figure 3c and Figure S5 in Supporting Information) and broadening (lower panel of Figure 3c and Figure S5 in Supporting Information), showing both the homogeneity of the initial quantum well emission on a microscale and the absence of lateral quantum confinement in this NW diameter range. The InGaN quantum disk emission wavelength is also very similar to the InGaN quantum well (Figure S6 in Supporting Information), confirming that the sublimation process does not modify the properties of the active layer. As can be seen in the μPL map of Figure 3b, the intensity however varies significantly from NW to NW, which constitutes the main flaw of the investigated sample. This is due to the disparity of material quality at the microscale and more specifically to the presence of threading dislocations that are known as non-radiative recombination centers (Figure S2 in Supporting Information). It is thus expected that this drawback is not intrinsic to the sublimation method but is rather dependent on the material quality of the original epilayer. It could thus be addressed by using more advanced epistacks with dislocation filtering designs or by growing the epilayers on a GaN homosubstrate.

Varying the sample temperature, we observe that individual NWs typically show a $\frac{I_{4K}}{I_{300K}} = 1.75$ quenching of the InGaN quantum disks photoluminescence from T = 4 K to T = 300 K (Figure 4a and b). The intensity quenching comes along with a drastic reduction in exciton lifetime in the quantum disk from $\tau_{4K} = 0.90\text{ns}$ to $\tau_{300K} = 0.22ns$, as observed by time-resolution microphotoluminescence (Figure 4c). This is consistent with an activation of faster non-radiative

recombination processes as temperature increases. The resulting quenching is actually smaller than recently reported values obtained in self-assembled InGaN NW quantum disks ($\frac{I_{4K}}{I_{300K}} > 10$).[30] This is not only due to the efficient confinement of carriers in InGaN heterostructures brought about by the large band offset and the well-known localization effect of InGaN,[31] but also to the high NW crystal quality obtained by the selective-area sublimation method (Figures 1f and 1g).

As often the case in InGaN heterostructures,[15] the localization effects due to both the InGaN thickness fluctuations (Figure 1g) and the InGaN alloying disorder lead to three-dimensional quantum confinement. As a result, we can distinguish quantum-dot-like emission of discrete states at low excitation density and low temperature (Figure 5a and b). Most of the quantum-dot-like emission behaves as single excitons with a linear dependence of the emission intensity as a function of the excitation density (Figure 5 c). At low excitation density, some quantum dot peaks can be resolution-limited (Figure 5 b and d) with the narrowest peak linewidth equal to 750 μeV, but a significant number of linewidths are actually larger than 1 meV (Figure 5 c). They are thus broadened by spectral diffusion, *i.e.* by the influence of the electrostatic environment fluctuations on the emission wavelength, as is often the case in polar group-III nitride quantum dots.[32,33] Overall, the linewidths observed here are very similar to what has been obtained in InGaN quantum dots embedded in NWs obtained through bottom-up approaches.[15,34] On the second timescale (see Figure S7 in Supporting Information), time-dependence measurements of the quantum dot peaks do not show the jittering that is sometimes observable in GaN[32,35] and InGaN[36] quantum dots. It means that the carrier trapping/detrapping processes that drive the electrostatic environment fluctuations only take place on shorter time scales, typically a few hundreds of nanoseconds as previously reported in InGaN quantum dots.[36]

The time-resolved μPL of single quantum dots at low excitation and T = 4 K reveals single exponential decays. The radiative lifetimes inferred from this exponential decay varies widely between 0.98 ns and 9 ns with a mean value $\overline{\tau_r} = 4.5 \pm 3ns$. Indeed, because electron-hole overlap in polar III-nitrides is greatly affected by small changes in geometry and confinement potential, the radiative lifetime is particularly sensitive to the random nature of the InGaN quantum dot formation. The radiative lifetimes observed here are however in line with previously reported values for InGaN quantum dot.[15,34,36] One would also notice that quantum dot lifetimes are consistently longer than the quantum disk lifetime measured in Figure 4: this is because the built-in electric field taking place in the polar InGaN quantum disk is screened at the high excitation density used to probe the quantum disk but not at the low excitation density used to probe the quantum dots.

The quantum dot single exciton emission can be observed up to high temperatures (T = 133 K) (Figure 5a) due to the efficient carrier confinement mentioned earlier. As the temperature increases however, phonon coupling comes into play and the emission linewidth of single excitons broadens with a typical E_a = 34 meV activation energy (Figure 5e). As the temperature increases another phenomenon occurs: carriers escape from the quantum dots and non-radiative recombination processes are activated, so that the integrated intensity of the single exciton emission quenches and finally disappears in the quantum disk emission background at T > 133 K (Figure 5f). Let us mention however that, as can readily be seen in Figure 5a, the activation energy of the quenching (E_b = 14 meV in Figure 5f) and the highest temperature at which the exciton can be observed varies widely from quantum dot to quantum dot, depending on their depths as well as their spectral and spatial density.

In order to gain more insight into the single quantum dot optical properties, we finally perform some polarization measurements on 39 single exciton peaks arising from various NWs. They present wide variations in terms of both the orientation and degree of linear polarization (Figure 5h and i). This stems from the various shape anisotropy of the quantum dot brought about by the random InGaN alloying disorder in the quantum disk.[37] Polarization measurements do not show any clear signature of fine-structure splitting, which means that we observe either charged excitons or neutral exciton exhibiting a splitting smaller than our setup resolution. The latter is actually consistent with results obtained by Amloy *et al.* showing fine-structure splitting smaller than 400 μeV in InGaN/GaN quantum dots.[37]

Photonic Integration. The intense room-temperature luminescence of the GaN band-edge and InGaN quantum disks, the signature of quantum dot emission at low excitation density and the fine control of their geometry make such NWs exciting candidates for integration in photonic platforms. First, by tuning the shape and diameter of NWs, we can obtain on the same wafer not only so-called subwavelengths NWs, *i.e.* NWs too thin to guide light (see Figure S8 in Supporting Information), but also NWs thick enough to confine ultraviolet and visible photons and to enable the formation of Fabry-Pérot modes. Owing to the poor index contrast between GaN and AlGaN and to the limited thickness of the AlGaN layer, the reflection at the AlGaN/GaN interface is negligible and cannot allow for the formation of NW Fabry-Pérot cavity modes on the as-sublimated wafer. Interferences observed in the photoluminescence spectra of Figure 3a are actually due to the reflection of light at the GaN/air and GaN/sapphire interfaces and can already be observed in the as-grown substrate (Figure S6 in Supporting Information). To evidence light confinement and the presence of intrinsic Fabry-Pérot modes in NWs, we transfer them on a SiN on silicon substrate by dry contact (Figure 6a). In such a configuration, mode

calculations at λ = 420 nm (see upper inset of Figure 6a and Figure S8 in Supporting Information) show the existence of confined photonic modes for diameters larger than 103 nm and 140 nm in triangular and hexagonal NWs respectively. Whereas subwavelength NWs present μPL spectra devoid of cavity modes, thicker NWs such as the one shown in Figure 6a (triangular section, δ = 114nm, L = 4 μm) present periodic peaks covering the whole blue-violet emission range (Figure 6b), which is typical of Fabry-Pérot resonances. The experimentally observed mode spacing $\Delta\lambda_{exp} = 8.5nm$ is actually in good agreement with the expected spacing $\Delta\lambda_{th} = \frac{\lambda^2}{2L}(n_{eff} - \lambda\frac{dn_{eff}}{d\lambda})^{-1} = 8.1nm$ derived from effective index calculations at λ = 420 nm (Figure S8 in Supporting Information). For an excitation laser spot focused at the center of the NW, the NW exhibits not only an intense blue emission at the InGaN quantum disk position but also at both end-facets of the NW (lower inset of Figure 6a). This confirms that the light emitted from the quantum disk is allowed to propagate along the NW before to partially escape at the end-facets.

If subwavelength NWs cannot intrinsically support photonic Fabry-Pérot modes, one can form optical nanocavities by integrating them in either dielectric photonic crystal[38-41] or plasmonic[10-12] platforms, thus obtaining even smaller cavity mode volumes. We here propose to realize InGaN/GaN NW-induced nanocavities in slotted SiN photonic crystal waveguides, an approach that has already been implemented in the near-ultraviolet range with ZnO NWs[39] but has yet to be demonstrated with group-III nitrides. A fabricated NW-induced nanocavity is displayed in Figure 6c after transfer to a SiN photonic crystal platform and insertion of the NW in the slot by nanomanipulation: one can observe that the NW diameter is smaller than the photonic mode cutoff (calculated in Figure S8) and its length is shorter than the initially fabricated NWs due to unintentional cleaving during the transfer and nanomanipulation process. Such an InGaN/GaN

NW-induced nanocavities can support a fundamental mode presenting a quality factor as high as $Q_{th} = 1.3\times10^3$ for a mode volume $V_m = 1.8\ (\lambda/n_{GaN})^3$ according to three-dimensional finite-difference time-domain calculations (Figure 6d). The room temperature μPL spectra of such nanocavities present sharp peaks in the visible range corresponding to the fundamental mode at $\lambda = 432$ nm and higher order modes at shorter wavelengths (Figure 6b). While a subwavelength NW transferred on SiN presents an emission linearly polarized along the NW, the fundamental cavity mode presents a cross-polarized behavior (see insets of Figure 6b). This confirms the origin of the peak as it is in agreement with 3D-FDTD calculations showing that the electric field component polarized perpendicular to the NW axis has the largest overlap with the NW.[41] The insertion of subwavelength NWs with lengths shorter than 2 microns into photonic crystals of various lattice constants shows that nanocavity modes can be observed across the near-ultraviolet and blue-violet range with experimental quality factors as high as $Q_{exp} = 1.2\times10^3$ (Figure 6e). This extension of our NW-induced nanocavity design from ZnO[41] to InGaN/GaN NWs incidentally shows the versatility of this hybrid nanophotonic platform that can be used with multiple NW materials across large wavelength ranges.

Lasing. If the gain of a single InGaN quantum disk is not sufficient to overcome optical losses in Fabry-Pérot NWs and NW-induced nanocavities, we however demonstrate that it is possible to reach room-temperature lasing in a Fabry-Pérot NW, using GaN as the gain medium. To that end, we realize power-dependent μPL measurements (Fig. 7a) on a single NW with a hexagonal cross-section, a diameter $\delta = 119$ nm and a length $L = 4$ μm. Similarly to what was observed previously in the visible range (Fig. 6b), the spectra present periodic peaks attributed to Fabry-Pérot resonances in the near-ultraviolet range close to the GaN band-edge. The observed peak spacing $\Delta\lambda_{exp} = 2.5nm$ is once again in good agreement with the expected spacing $\Delta\lambda_{th} =$

$2.35nm$ derived from effective index calculations at λ = 370 nm (see Figure S8 in Supporting Information). As power increases, the Fabry-Pérot resonance at λ = 370 nm exhibits a superlinear behavior highlighted by the S-shape of its light-light curve while other Fabry-Pérot modes increase linearly up to threshold and flatten thereon (Fig. 7b). This behavior is indicative of lasing action at λ = 370 nm with a clear threshold at peak power $P_{th} = 3MW.cm^{-2}$ and a clamping of spontaneous emission above threshold. Lasing action is further evidenced by the wavelength blue-shift (Fig. 7c) as well as the drastic reduction of the lasing mode linewidth at threshold (Fig. 7d). The lasing threshold $P_{th} = 3MW.cm^{-2}$ is very similar to values obtained in Fabry-Pérot NWs fabricated by plasma etching followed by chemical cleaning,[8] which confirms the high quality of the sublimation process to realize optically active NWs. An analysis of the light-light curve (see Methods) gives us an estimate of the coupling factor in this lasing NW $\beta = 6 \times 10^{-3}$. This value is in line with the coupling factor range $\beta \sim 2 \times 10^{-3}$ to 1.5×10^{-2} found in Fabry-Pérot NW lasers based on various material systems.[42,44] It translates the multimode nature of the Fabry-Pérot cavity as well as a rather large mode volume if compared to plasmonic[10-12] and photonic crystal[38-41] nanocavities.

CONCLUSION. We have demonstrated that selective-area sublimation together with electron-beam lithography can be a powerful and versatile method to realize precisely defined GaN-based NW arrays in a top-down approach. We have shown that it not only allows for high yield and homogeneity on a macroscale, but also for a fine nanoscale control in terms of position, shape and dimensions. Despite this top-down approach, we have been able to demonstrate the high material and optical quality of NWs, which is highlighted by (i) the intense room-temperature luminescence of InGaN/GaN NW quantum disk arrays and (ii) the signature of quantum dots matching state-of-the art InGaN quantum dots obtained through bottom-up methods.[15,34,36] This

high optical quality is evidence of the clear advantage of selective-area sublimation over top-down plasma etching techniques that induce significant material damage and require a slow and burdensome post-processing treatment to recover optoelectronic quality.[8] Taking advantage of the ultra-high vacuum environment in which the sublimation is carried out, it also means that the sublimation method will allow for the realization of more complex NW designs, including core-shell and hollow-core structures as well as radial heterostructures. The great potential of such a strategy has just been highlighted by Sun *et al.*[45] who used GaN sublimation and regrowth to adjust the diameter of InGaN quantum disks embedded in self-assembled GaN NWs and to tailor the optical properties of single-photon sources. To further highlight the versatility of our fabrication method and its potential for nanophotonic applications, we have shown that it is possible to couple such NWs with optical cavities: we have demonstrated the existence of intrinsic Fabry-Pérot resonances in thick NWs that lead to room-temperature lasing in the near-ultraviolet range, and we have integrated subwavelength NWs into a hybrid nanophotonic platform. Note that if the nanomanipulation approach used here to form NW-induced cavities in photonic crystals is not the most efficient, there exists exciting perspectives with wafer-scale NW assembly methods that allow deterministic positioning.[46] It will also be possible to expand on this work by forming intrinsic NW Fabry-Pérot cavities directly on the wafer without the need for transfer: this can be done either by relying on the index contrast with the sapphire substrate, similarly to Behzadirad *et al.*[8] and Damilano *et al.*,[26] or by growing a bottom Bragg mirror, as routinely done in vertical-cavity surface-emitting lasers and polariton lasers.[47] This would open a path to the realization of integrated arrays of NW-based photon and polariton nanolasers emitting in the ultraviolet and visible ranges.

METHODS

Nanowire fabrication. The initial InGaN/GaN stack is grown by molecular beam epitaxy on a 2-inch c-plane sapphire substrate. A 65-nm-thick SiN hard-mask is then deposited on the top-surface by cathodic sputtering. A 120-nm-thick negative-tone resist is spin-coated on the SiN layer and the mesas are defined by electron beam lithography, using a 100 kV acceleration voltage. After development, the patterns are subsequently transferred to the SiN layer by reactive ion etching using a SF_6 plasma. The sample is then reintroduced into the ultra-high-vacuum molecular beam epitaxy reactor and the sample is heated up to 925 °C in order to carry out the sublimation process. The process is monitored in real-time with a reflection high-energy electron diffraction apparatus.

TEM measurements. For TEM observations, the samples are prepared by focused ion beam using a 30kV acceleration voltage and sliced into 100 nm thick lamella. The NW cross-section is observed along the $[0001]$ direction by conventional TEM in a field emission electron microscope. The InGaN quantum well is observed along the $[1\bar{1}00]$ direction by annular bright field scanning TEM in an atomic resolution analytical electron microscope. Both microscopes use a 200kV acceleration voltage.

Optical measurements. NWs are excited by a continuous-wave laser emitting at 320 nm for steady-state measurements. For time-resolved measurements, we use a PicoQuant laser diode emitting at 375 nm with a 40MHz repetition rate. NW lasing experiments are carried out using a Teem Photonics pulsed laser emitting at 266 nm with a 1 kHz repetition rate and a 0.35 ns pulse width. The lasers are focused with a Mitsutoyo microscope objective dedicated to the ultraviolet range with a 50-fold magnification and a 0.42 numerical aperture. The emitted signal is collected in a confocal configuration and focused on either a visible camera or a 1200 grooves/mm grating through a 30-micron slit. After dispersion on the grating, the signal is directed to a charge-

coupled device camera for time-integrated measurements. For time-resolved measurements, the signal is instead coupled to a 50-micron large multimode fiber connected to a Hamamatsu photon multiplier and a time-correlated photon counter. Polarization properties are investigated by adding a polarization analyzer on the signal collection path, just after the microscope objective. The spectral resolution in the considered wavelength range is 70 pm. The time resolution is limited by both the PicoQuant diode laser pulse width (~40ps) and the photon multiplier resolution (~210ps).

Mode calculations. The photonic modes guided in thick NWs are calculated with the Lumerical Mode Solutions toolbox. Photonic crystal nanocavity calculations are carried out by 3D-FDTD calculations using our home-built algorithm. The refractive indices used for GaN, SiN and Si in the calculations are extracted from references 48 to 50.

Photonic platform fabrication. SiN wafers are grown by plasma-enhanced chemical vapor deposition on silicon (100). The SiN thickness is 108nm. The photonic crystal platform is realized in the SiN layer by successive electron beam lithography and plasma etching steps successively for alignment markers, photonic crystals and grooves. The silicon substrate below the photonic crystal slab is then etched in a KOH solution at 65°C. More details can be found in reference 39.

Nanowire manipulation. NWs are transferred from their original substrate to the SiN platform by dry contact under a 2 $N.cm^{-2}$ pressure. For the photonic crystal platform, the NWs need to be manipulated and inserted into slots. This process is realized in an atomic force microscopy apparatus using a silicon cantilever. The cantilever presents a tip with an 8 nm radius, a 42 N/m

spring constant and is operated in contact mode at a 500 nm/s velocity. More details on the nanomanipulation process can be found in references 39 and 40.

Light-Light curve analysis. The light-light curve analysis of the NW laser is based on the following rate equation system:

$$\frac{dn}{dt} = p(t) - v_g g s(n - n_0) - \gamma_r n - \gamma_{nr} n \qquad (1)$$

$$\frac{ds}{dt} = \Gamma_{NW} v_g g s(n - n_0) + \beta \Gamma_{NW} \gamma_r n - \gamma_{ph} s \qquad (2)$$

with $\mathrm{p(t)} = p_0 e^{-\frac{(t-t_0)}{\Delta t^2}}$ the pump density, s and n the photon and carrier densities, n_0 the carrier density at transparency, g the differential gain, γ_r and γ_{nr} the radiative and nonradiative decay rates, Γ_{NW} the confinement factor of the mode into the NW, v_g the group velocity of the mode, γ_{ph} the photon loss rate of the cavity mode and β the coupling factor. p_0 is the peak pump density and $\Delta\mathrm{t} = 0.35\mathrm{ns}$ the pulse width of the laser. $\mathrm{g} = 3.3 \times 10^{-16} cm^2$ and $n_0 = 8 \times 10^{18} cm^{-3}$ are extracted from reference 51. Regarding the carrier decay rates, we consider the decay lifetimes found in the literature[52,53] *i.e.* $\tau_r = 1ns$ and $\tau_{nr} = 50ps$. $\Gamma_{NW} = 0.71$ and $v_g = 4.1 \times 10^{10} cm/s$ are estimated directly from the photonic mode calculations detailed above.

ASSOCIATED CONTENT

Supporting Information. The Supporting Information provides additional fabrication, optical measurement and simulation data. The following files are available free of charge via the Internet at http://pubs.acs.org.

Additional photonic mode calculations, structural and optical measurements as well as data analyses (.PDF)

AUTHOR INFORMATION

Corresponding Authors

* Email: sylvain.sergent@lab.ntt.co.jp

** Email: benjamin.damilano@crhea.cnrs.fr

Author Contributions

S.S., B.D. and S.V. designed the samples and experiments. S.V. and B.D. fabricated the NWs with the assistance of S.S. for the electron beam lithography step and the assistance of S.C. for the SiN mask deposition. S.S., B.D. and S.V. performed the structural characterizations of NWs. T.T. and S.S. fabricated the SiN photonic platform. S.S. conducted the optical experiments with the assistance of M.T. and carried out photonic mode calculations with the assistance of H.T. S.S. analyzed the data and wrote the manuscript through contributions of all authors. M.N. supervised the project from the NTT end. All authors have given approval to the final version of the manuscript.

Notes

The authors declare no competing financial interests.

Funding Sources

This work has been supported by the JSPS KAKENHI Grant Number 15H05735 and the French National Research Agency (ANR) through the project NAPOLI (ANR-18-CE24-0022).

ABBREVIATIONS

NW, nanowire; RHEED, reflection high-energy electron diffraction; 3D-FDTD, three-dimensional finite-difference time-domain calculations; SEM. Scanning electron microscope; TEM. Transmission electron microscopy; μPL, Microphotoluminescence.

REFERENCES

(1). Kikuchi A.; Kawai M.; Tada M.; Kishino K. InGaN/GaN Multiple Quantum Disk Nanocolumn Light-Emitting Diodes Grown on (111) Si Substrate. *Japanese Journal of Applied Physics* **2004**, 43, L1524-L1526.

(2). Guan N ; Dai X. ; Messanvi A.; Zhang H.; Yan J.; Gautier E.; Bouerol C.; Julien F.H.; Durand C.; Eymery J.; Tchernycheva M. Flexible White Light Emitting Diodes Based on Nitride Nanowires and Nanophosphors. *ACS Photonics* **2016**, 3, 597-603.

(3). Nami, M. ; Feezell, D. Optical properties of Ag-coated GaN/InGaN axial core-shell nanowire light-emitting diodes. *Journal of Optics* **2015**, 17, 025004.

(4). Mohajerani, M.S.; Muller, M.; Hartmann, J. ; Zhou, H.; Wehmann, H.H.; Veit, P; Bertram, F.; Christen, J.; Waag, A. Direct correlation of structural and optical properties of three-dimensional GaN/InGaN core/shell micro-light emitting diodes. *Japanese Jounal of Applied Physics*, **2016**, 55, 05FJ09.

(5). Nami, M.; Stricklin, I.E.; DaVico, K.M.; Mishkat-Ul-Masabih, S.; Rishinaramangalam, A.K.; Brueck, S.R.J.; Brener, I.; Feezell D.F. Carrier dynamics and electro-optical characterization of high performance GaN/InGaN core-shell nanowire light-emitting diodes. *Scientific Reports* **2018**, 8, 501.(6). Zhang H.; Dai X. ; Guan N ; Messanvi A.; Neplokh V.; Piazza V.; Vallo M.; Bouerol C.; Julien F.H.; Babichev A.; Cavassilas N.; Bescond M. ;

Michelini F.; Foldyna M.; Gautier E.; Durand C.; Eymery J.; Tchernycheva M. Flexible Photodiodes Based on Nitride Core/Shell p–n Junction Nanowires. *ACS Applied Materials & Interfaces* **2016**, 8, 26198-26206.

(7). Heo, J.; Guo, W.; Bhattacharya, P. Monolithic single GaN nanowire laser with photonic crystal microcavity on silicon. *Appl. Phys. Lett.* **2011**, 98, 021110.

(8). Behzadirad M.; Nami M.; Wostbrock N.; Kouhpanji M.R.Z.; Feezell D.F.; Brueck S.R.J.; Busani T. Scalable Top-Down Approach Tailored by Interferometric Lithography to Achieve Large-Area Single-Mode GaN Nanowire Laser Arrays on Sapphire Substrate. *ACS Nano* **2018**, 12, 2373-2380.

(9). Li, Q.; Wright, J. B.; Chow, W.W.; Luk, T.S.; Brener, I.; Lester, L.F.; Wang, G. T. Single-mode GaN nanowire lasers. *Optics Express* **2012**, 20, 17873.

(10). Lu Y.-J.; Kim J.; Chen H.-Y.; Wu C.; Dabidian N.; Sanders C.E.; Wang C.-Y.; L M.-Y.; Li B.-H;. Qiu X.; Chang W.-H.; Chen L.-J.; Shvets G.; Shih C.K.; Gwo S. Plasmonic Nanolaser Using Epitaxially Grown Silver Film. *Science* **2012**, 337, 450-453.

(11). Zhang, Q.; Li, G. Liu, X., Qian, F. Li, Y., Sum, T. C ; Lieber, C. M. ; Xiong, Q. A room temperature low-threshold ultraviolet plasmonic nanolaser. *Nature Communications* **2012**, 5, 4953.

(12). Lu Y.-J.; Wang C.-Y.; Kim J.; Lu M.-Y.; Chen H.-Y.; Chen Y.-C.; Chang W.-H.; Chen L.-J.; Stockman M.I..; Shih C.K.; Gwo S. All-Color Plasmonic Nanolasers with Ultralow Thresholds: Autotuning Mechanism for Single-Mode Lasing. *Nano Letters* **2014**, 14, 4381-4388.

(13). Das A.; Heo J.; Jankowski M.; Guo W.; Zhang L.; Deng H.; Battacharya P. Room Temperature Ultralow Threshold GaN Nanowire Polariton Laser. *Phys. Rev. Lett.* **2011**, 107, 066405.

(14). Holmes M.; Choi, K.; Kako, S.; Arita, M.; Arakawa, Y. Room-temperature triggered single photon emission from a III-nitride site-controlled nanowire quantum dot. *Nano Letters* **2014**, 14, 982-986.

(15). Deshpande S.; Heo J.; Das A.; Bhattacharya P. Electrically driven polarized single-photon emission from an InGaN quantum dot in a GaN nanowire. *Nature Communication* **2013**, 14, 1675.

(16). Songmuang, R.; Landré, O.; Daudin, B. From nucleation to growth of catalyst-free GaN nanowires on thin AlN buffer layer. *Applied. Phys. Lett.* **2007**, 91, 251902.

(17). Bertness, K.A.; Sanford, N.A.; Davydov, A.V. GaN nanowires grown by molecular beam epitaxy. *IEEE J. Sel. Topics in Quantum Electron.* **2011**, 17, 847-858.

(18). Tourbot G.; Bougerol, C.; Grenier, A.; Den Hertog, M.; Sam-Giao, D.; Cooper, D.; Gilet, P.; Gayral, B.; Daudin, B. Structural and optical properties of InGaN nanowire heterostructures grown by PA-MBE. *Nanotechnology* **2011**, 22, 075601.

(19). Alloing, B.; Vézian, S.; Tottereau, O.; Vennegues, P.; Beraudo, E.; Zuniga-Perez J. On the polarity of GaN micro- and nanowires epitaxially grown on sapphire (0001) and Si (111) substrates by metal organic vapor phase epitaxy and ammonia-molecular beam epitaxy. *Appl. Phys. Lett.* **2011**, 98, 011914.

(20). Hersee, S. D.; Sum, X.; Wang X. The controlled growth of GaN nanowires. *Nano Lett.* **2006**, 6, 1808-1811.

(21). Choi, K.; Arita, M.; Arakawa Y. Selective-area growth of thin GaN nanowires by MOCVD. *J. of Cryst. Growth* **2012**, 357, 58-61.

(22). Schimpke, T.; Lugauer, H.-J.; Avramescu, A.; Varghese, T. ; Koller, A. ; Hartmann, J. ; Ledig, J.; Waag, A.; Strassburg, M. Position-controlled MOVPE growth and electro-optical characterization of core-shell InGaN microrod LEDs. *Proc. SPIE 9768, Light-Emitting Diodes: Materials, Devices, and Applications for Solid State Lighting XX*, **2016**, 97680T.

(23). Nami, M.; Eller, R.F.; Okur, S.; Rishinaramangalam, A.K.; Liu, S.; Brener, I.; Feezell D.F. Tailoring the morphology and luminescence of GaN/InGaN core-shell nanowires using bottom-up selective-area epitaxy. *Nanotechnology* **2016**, 28, 025202.

(24). Chen, W.; Lin, J.; Hu, G.; Han, X; Liu, M.; Yang, T.; Wu, Z.; Liu, Y.; Zhan, B. GaN nanowire fabricated by selective wet-etching of GaN micro truncated-pyramid *J. of Cryst. Growth* **2015**, 428, 168-172.

(25). Li, Q.; Westlake, K. R.; Crawford, M. H.; Lee, S. R.; Koleske, D. D.; Figiel, J.; Cross, K. C.; Fathololoumt; S.; Mi, Z.; Wang; G. W. Optical performance of top-down fabricated InGaN/GaN nanorod light emitting diode array. *Optics Express* **2011**, 19, 25528-25534.

(26). Damilano B.; Vézian S.; Brault J.; Alloing B.; Massies J. Selective Area Sublimation: A Simple Top-down Route for GaN-Based Nanowire Fabrication. *Nano Letters* **2016**, 16, 1863-1868.

(27). Damilano B.; Vézian S.; Portail, M.; Alloing, B.; Brault J.; Courville, A.; Brandli, V.; Leroux, M.; Massies J. Selective Optical properties of InGaN/GaN quantum disks obtained by selective-area sublimation. *Journal of Crystal Growth* **2017**, 477, 262-266.

(28). Damilano B.; Coulon. P.-M.; Vézian S.; Brändli, V.; Duboz, J.-Y.; Massies, J.; Shields, P. A. Top-Down Fabrication of GaN Nano-Laser Arrays by Displacement Talbot Lithography and Selective Area Sublimation. *Appl. Phys. Express* **2019**, 12, 045007.

(29). Brière, G.; Ni, P.; Héron, S.; Chenot, S., Vézian S.; Brändli, V.; Damilano B.; Duboz, J.-Y.; Iwanaga, M.; Genevet, P. An Etching-Free Approach Toward Large-Scale Light Emitting Metasurfaces. *Adv. Opt. Mater.* **2019**, 1801271.

(30) Bao, W.; Su, Z.; Zheng, C., Ning, J; Xu, S. Carrier localization effects in InGaN/GaN multiple quantum wells LED nanowires: luminescence quantum efficiency improvement and "negative" thermal activation energy. *Scientific Reports* **2016**, 6, 34545.

(31). Chichibu, S.; Azuhata, T.; Sota, T. ; Nakamura, S. Spontaneous emission of localized excitons in InGaN single and multiquantum well structures. *Applied Physics Letters* **1996**, 69, 4188.

(32). Bardoux, R.; Guillet, T. ; Lefebvre, P. ; Tialercio, T.; Bretagnon, T. ; Rousset S. ; Semond, F. Photoluminescence of single GaN⁄AlN hexagonal quantum dots on Si(111): Spectral diffusion effects. *Physical Review B* **2006**, 74, 105319.

(33). Holmes, M. J.; Kako, S. ; Choi, K.; Arita, M.; Arakawa, Y. Spectral diffusion and its influence on the emission linewidths of site-controlled GaN nanowire quantum dots. *Physical Review B* **2015**, 92, 115447.

(34). Gačević, Ž.; Holmes, M.; Chernysheva, E.; Müller, M.; Torres-Pardo, A.; Veit, P.; Bertram, F.; Christen, J.; Calbet J. M. G.; Arakawa, Y.; Calleja, E.; Lazić S. Emission of linearly polarized single photons from quantum dots contained in nonpolar, semipolar and polar sections of pencil like InGaN/GaN nanowires. *ACS Photonics* **2017**, 4, 657.

(35). Sergent, S.; Kako, S.; Bürger, M.; As, D. J.; Arakawa, Y. Narrow spectral linewidth of single zinc-blende GaN/AlN self-assembled quantum dots. *Applied Physics Letters* **2013**, 103, 151109.

(36). Gao, K; Springbett, H.; Zhu, T.; Oliver, R. A.; Arakawa, Y.; Holmes M. J. Spectral diffusion time scales in InGaN/GaN quantum dots. *Applied Physics Letters* **2019**, 114, 112109.

(37). Amloy, S.; Chen, Y. T.; Karlsson, K. F.; Chen, K. H.; Hsu, H. C.; Hsiao, C. L.; Chen, L. C.; Holtz P. O. Polarization-resolved fine-structure splitting of zero-dimensional InGaN excitons. *Physical Review B* **2011**, 83, 201307(R).

(38) Birowosuto, M. D.; Yokoo, A.; Zhang, G.; Tateno, K.; Kuramochi, E.; Taniyama, H.; Takiguchi, M.; Notomi, M. Movable high-Q nanoresonators realized by semiconductor nanowires on a Si photonic crystal platform. *Nat. Mater.* 2014, 13, 279.

(39). Sergent, S.; Takiguchi M.; Tsuchizawa T.; Yokoo, A.; Taniyama, H.; Kuramochi, E.; Notomi, M. Nanomanipulating and Tuning Ultraviolet ZnO-nanowire-induced photonic crystal nanocavities. *ACS Photonics* **2017**, 4, 1040-1047.

(40). Sergent, S.; Takiguchi M.; Tsuchizawa T.; Taniyama, H.; Notomi, M. ZnO-nanowire-induced nanocavities in photonic crystal disks. *ACS Photonics* **2019**, 6, 1132-1138.

(41). Sergent, S.; Takiguchi M.; Taniyama, H.; Shinya, A.; Kuramochi, E.; Notomi, M. Design of nanowire-induced nanocavities in grooved 1D and 2D SiN photonic crystals for the ultra-violet and visible ranges. *Optics Express* **2016,** 24, 26792.

(42) Saxena, D.; Mokkapati, S.; Parkinson P.; Jiang, Nan; Gao,Q.; Tan, H. H.; Jagadish, C. Optically pumped room-temperature GaAs nanowire lasers. *Nat. Phot.* 2013, 7, 963.

(43) Tatebayashi, J.; Kako, S.; Ho, J.; Ota, Y.; Iwamoto, S., Arakawa, Y. Room-temperature lasing in a single nanowire with quantum dots. *Nat. Phot.* 2015, 9, 501.

(44) Zhang, G.; Takiguchi, M.; Tateno, K.; Tawara, T.; Notomi, M.; Gotoh, H. Telecom-band lasing in single InP/InAs heterostructure nanowires at room-temperature. *Sc. Adv.* 2019, 5, eaat8896.

(45) Sun, X.; Wang, P.; Sheng, B.; Wang, T.; Chen, Z.; Gao, K.; Li, M.; Zhang, J.; Ge, W.; Arakawa, Y.; Shen, B.; Holmes, M.; Wang, X. Single-photon emission from a further confined InGaN/GaN quantum disk via reverse-reaction growth. *Quantum Engineering* 2019, 1, e20.

(46) No, Y.-S.; Xu, L.; Mankin, M. N.; Park, H.-G. Shape-controlled assembly of nanowires for photonic elements. *ACS Photon.* 2016, 3, 2285.

(47). Zuniga-Perez, J.; Mallet, E.; Hahe, R.; Rashid, M. J.; Bouchoule, S.; Brimont, C.; Disseix, P., Duboz, J. Y.; Gommé, G. ; Guillet T. *et al.* Patterned Silicon Substrates: A Common Platform for Room Temperature GaN and ZnO Polariton Lasers. *Appl. Phys. Lett.* **2014**, 104, 241113.

(48). Antoine-Vincent, N.; Natali F.; Mihailovic M. ; Vasson A. ; Leymarie J. ; Disseix P. ; Byrne D. ; Semond F. ; Massies, J. *J. of Appl. Phys.* **2003**, 93, 5222.

(49). Luke, K.; Okawachi, Y.; Lamont, M. R. E.;Gaeta, A. L.; Lipson, M. Broadband mid-infrared frequency comb generation in a Si_3N_4 microresonator. *Optics Lett.* **2015**, 40, 4823.

(50). Palik, E. D. Handbook of optical constants. ed. Academic Press, Boston, **1985**.

(51). Meney, A. T.; O'Reilly, E. P. Theoretical of optical gain in ideal GaN heterostructure lasers. *Appl. Phys. Lett.* **1995**, 67, 3013.

(52). Monemar, B.; Paskov, P. P.; Bergman, J. P.; Pozina, G.; Toropov, A. A.; Shubina, T. V.; Malinauskas, T.; Usui, A. Transient photoluminescence of shallow donor bound excitons in GaN. *Phys. Rev. B* **2010**, 82, 235202.

(53). Harris, C. I.; Monemar, B.; Amano, H.; Akasaki, I. Exciton lifetimes in GaN and GaInN. *Appl. Phys. Lett.* **1995**, 67, 840.

For Table of Contents Use Only.

"**Subliming GaN into ordered nanowire arrays for visible and ultraviolet photonics**"

Authors: Sylvain Sergent, Benjamin Damilano, Stéphane Vézian, Sébastien Chenot, Masato Takiguchi, Tai Tsuchizawa, Hideaki Taniyama and Masaya Notomi.

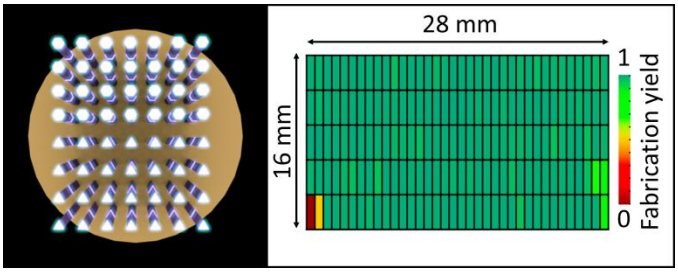

Schematic representation of light-emitting triangular and hexagonal nanowire arrays. Fabrication yield across the fabricated sample.